Materials Today Communications 36 (2023) 106684

Contents lists available at ScienceDirect

Materials Today Communications

journal homepage: www.elsevier.com/locate/mtcomm

First principles prediction of yield strength of body centered cubic structured high entropy alloys

Siming Zhang , Guofeng Wang *

Department of Mechanical Engineering and Materials Science, University of Pittsburgh, PA 15261, USA

ARTICLE INFO

Keywords:
High entropy alloys
First principles calculation
Generalized stacking fault energy
Peierls stress
Yield strength

ABSTRACT

High entropy alloys (HEAs) with a body centered cubic (bcc) crystal structure have emerged as potential high-performance structural materials due to their high strength at room and elevated temperatures. In this study, a computational approach, based on the revised Peierls-Nabarro model and using the inputs solely calculated from the first principles density functional theory, has been developed to predict the yield strength of bcc HEAs. Examining its accuracy and reliability, the developed computational approach was applied to four different types of bcc HEAs. The yield strength was predicted to be 1034 MPa for MoNbTaW, 1489 MPa for MoNbTaV, 1356 MPa for AlCoCrFeNi, and 1740 MPa for $AlCoCrFeNiZr_{0.3}$ alloy, respectively. These computational predictions are found to agree well with available experimental data. Moreover, the developed computational approach accurately quantifies the changes in the yield strength from MoNbTaW to MoNbTaV with a change of constituent W to V, and from AlCoCrFeNi to AlCoCrFeNiZr0.3 with addition of 6 at% Zr. Therefore, this first-principles based computational approach provides a way for expedite optimization on the mechanical properties of bcc HEAs across vast composition space.

1. Introduction

Owning to excellent mechanical properties, high entropy alloys (HEA) with a body-centered cubic (bcc) crystal structure have emerged as potential high-performance structural materials [1]. In a typical HEA, multiple principal metallic constituents in equal or nearly equal molar concentrations are processed to form homogeneously mixed solid solution with a simple crystal structure [2–4]. Bcc HEAs are most often found to exhibit relatively high intrinsic yield strengths over 1000 MPa [3,4] and retain reasonably good mechanical strength even at high temperature [4,5]. For example, MoNbTaW HEA with a single bcc solid solution phase could possess a yield strength of 1058 MPa at room temperature and maintain a yield strength of 552 MPa at 800 °C [6,7]. It was further reported that the yield strengths of MoNbTaWTi and MoNbTaWTiV HEAs could reach as high as 586 and 659 MPa at 1200 °C, respectively [8].

Moreover, it has been demonstrated that tuning chemical composition is an effective approach to tailor the mechanical properties of bcc HEAs. Adding Zr to AlCoCrFeNi alloy was found to increase the yield strength of $AlCoCrFeNiZr_x$ from 1330 MPa to 1987 MPa with the change of x from 0 to 0.5 [9]. In addition, gradually adding W into AlCrFeNiCu alloy was reported to change both the yield strength (from 1010.5 MPa (0 at% W), 998.4 MPa (1 at% W), to 1005.3 MPa (3 at% W)) and the maximum strength (from 1253.9 MPa (0 at% W), 1274.6 MPa (1 at% W), to 1287.9 MPa(3 at% W)) [10]. Furthermore, Huang et al. observed that, accompanying with decreasing content of Ta in $TiZrHfTa_x$ (x decreases from 1.0 to 0.5), the activated deformation mechanism in these bcc HEAs could change from deformation twinning, deformation-induced martensite, to martensite transformation twinning sequentially [11]. As a result, $TiZrHfTa_{0.6}$ and $TiZrHfTa_{0.5}$ alloys were found to have the best combination of strength and ductility [11].

So far, the composition design of HEAs is primarily carried out in an empirical trial-and-error way. A rational design of HEAs demands the development of computational approaches which can accurately predict the mechanical properties of bcc HEAs as a function of their chemical composition. Some progresses have been made on this forefront. For example, Ji et al. employed the first-principles density functional theory (DFT) method to calculate the elastic constants of a series of bcc $Ti_{65-x}Ta_{25}Nb_{10}Zr_x$ HEAs [12]. Their computational results showed a systematic decrease in the bulk modulus with the addition of Zr content in the HEAs. Moreover, Vazquez et al. have developed an efficient machine learning model to predict the elastic properties of bcc

* Corresponding author.
E-mail address: guw8@pitt.edu (G. Wang).

https://doi.org/10.1016/j.mtcomm.2023.106684
Received 22 May 2023; Received in revised form 14 July 2023; Accepted 15 July 2023
Available online 17 July 2023

NbMoTaWV-based HEAs over a large composition space [13]. Their model was trained using a database consisting of the DFT calculated elastic properties of the binary and ternary alloys and was able to predict the mechanical properties of HEAs from meaningful atomic features. Despite of these progresses, it is clearly noticeable that the reliable computational approach to predict the yield strength of bcc HEAs are rather scarce in the literature. To date, the only computational approach was developed by Maresca et al. considering solute-strengthening of edge dislocations in bcc HEAs and demonstrated to predict the yield strengths of MoNbTaW and MoNbTaVW alloys within 15% error range as compared to experimental values [14].

In a previous study [15], we have developed a computational approach to predict the yield strength of some select HEAs with a face-centered cubic lattice structure based on the revised Peierls-Naborro model [16] and using the DFT calculated generalized stacking fault energy (GSFE) curves. As compared to the experimentally measured values, the predicted yield strengths were found to differ only by 10.0% for CoFeNi, 2.5% for CoCrFeNi, 7.8% for CoCrFeCuNi, and 1.3% for RhIrPdPtNiCu HEAs [15]. In the present study, we extend the computational approach to predict the yield strength of bcc HEAs using (112) GSFE surface [17], considering the contributions from both edge and screw dislocations. Moreover, we have validated the reliability of the computational approach by examining its predictions for four different bcc HEAs (i.e., MoNbTaW, MoNbTaV, AlCoCrFeNi, and $AlCoCrFeNiZr_{0.3}$). More importantly, we quantified the effect of a composition change (i.e., change a constituent from W in MoNbTaW to V in MoNbTaV, and add Zr into AlCoCrFeNi to form $AlCoCrFeNiZr_{0.3}$) on affecting the yield strength of these HEAs.

2. Computational method

In this study, all the spin-polarized DFT calculations were performed using the Vienna ab initio simulation package (VASP) [18]. Plane wave basis associated with the projector augmented wave potentials [19] was employed. Specifically, the orbitals considered in the pseudopotentials were Mo (4p5s4d), Nb (4p5s4d), Ta (5p6s5d), W (5p6s5d), V (3p3d4s), Al (3s3p), Co(3d4s), Cr (3p3d4s), Fe (3d4s), Ni (3p3d4s), and Zr (4s4p5s4d). The plane wave energy cut-off energy was set to be 500 eV. The generalized gradient approximation (GGA) with the Perdew-Burke-Ernzerhof (PBE) [20] functional was used to evaluate the exchange-correlation energy. In the calculations, the total energy of each system was converged within 10^{-6} eV. In bulk crystal calculations, we used an orthogonal simulation cell containing 72 atoms to model MoNbTaW and MoNbTaV HEAs, and an orthogonal simulation cell containing 80 atoms to model AlCoCrFeNi and $AlCoCrFeNiZr_{0.3}$ HEAs. 3 × 4 × 4 and 3 × 4 × 5 Monkhorst-Pack k-point [21] grids were used in these 72- and 80-atom bulk crystal calculations, respectively.

In GSFE surface calculations, we constructed various (112) stacking faults of bcc crystal in a simulation cell spanned along $[\bar{1}\bar{1}1]$, $[1\bar{1}0]$, and [112] directions and containing sequentially packed (112) atomic layers (eight atoms each layer). In the simulation cells, a vacuum region of 12 Å thick was added in the [112] direction normal to the (112) layers to minimize the influence of periodic images. The GSFE surface was predicted by calculating the energies of various slab cells in which, relative to the bottom half crystal, the top half crystal slips simultaneously along $[\bar{1}\bar{1}1]$ direction up to a full Burgers vector of $\vec{b_1}$= a/2 < 111 > and along $[1\bar{1}0]$ direction up to a full Burgers vector of $\vec{b_2}$= a/2 < 110 > . During structural optimization, the positions of the two atomic layers on both the top and bottom of the slab were fixed whereas the positions of the other atoms were allowed to relax only in the [112] direction normal to the stacking fault. The stacking fault energies were computed as the energy difference per area between the slab model containing a stacking fault and the corresponding reference slab free of stacking fault. A Monkhorst-Pack k-point grid of 5 × 4 × 1 was used for these (112) GSFE surface calculations. All the structures were fully relaxed until the residual force acting on each atom was lower than 0.01 eV/Å.

3. Results and discussion

3.1. Theorem

The plastic deformation and behavior of conventional bcc metals at low temperature are believed to be primarily controlled by the mobility of screw dislocations via a kink-pair mechanism involving the nucleation and propagation of kinks along the screw dislocation [22]. In contrast to that in conventional bcc metals, the plastic deformation in some example bcc HEAs (such as, MoNbTi, NbTaTiV, and CrMoNbV alloys) was revealed to be mostly controlled by the slip of edge dislocations which led to the observed high-temperature strength retention in these HEAs [23,24]. Moreover, Lee et al. observed a/2 < 111 > type of dislocations on {110} and {112} slip planes of the deformed NbTaTiV and CrMoNbV HEAs using transmission electron microscopy [24]. This experimental observation is consistent with the predictions from large-scale molecular dynamics (MD) simulation on the bcc AlCoCrFeNi HEA nanopillars under uniaxial compression [25]. In the MD simulations, Zhang et al. found that a/2 < 111 > type full dislocations were nucleated from the free surface, slipped on {110}, {112}, or {123} planes, and interacted/reacted with each other [25].

Consequently, we consider the slip of the dislocations with both screw and edge characters as the primary deformation mechanism in bcc HEAs in this work. In bcc crystal, both full dislocations with Burger vectors of $\vec{b_1}$=a/2 < 111 > (pure screw) and $\vec{b_2}$=a/2 < 110 > (pure edge) would contribute the slip within a (112) slip plane [16,17,26]. We assume that the displacement caused by the dislocation has a form of $u(x) = \frac{b}{\pi}\tan^{-1}\frac{x}{\xi}+\frac{b}{2}$, where x represents the distance to the dislocation line along the Burgers vector direction (<111 > or <110 >) within a (112) plane, b is the length of the Burgers vector, and ξ is the dislocation width [16,27].

In the Peierls model based on dislocations containing both screw and edge components, the GSFE surface over a (112) plane in a cubic crystal could be expressed in an expansion of two-dimensional Fourier series [27]:

$$\begin{aligned}\gamma(u_y,u_z) = {} & c_0 + c_1\left[\cos 2pu_y\right] + c_2\left[\cos\left(pu_y+qu_z\right)+\cos\left(pu_y-qu_z\right)\right] \\ & + c_3\left[\cos 2qu_z\right] + c_4\left[\cos 4pu_y\right] + c_5\left[\cos\left(3pu_y+qu_z\right)+\cos\left(-3pu_y\right.\right. \\ & \left.\left.+qu_z\right)\right] + c_6\left[\cos\left(2pu_y+2qu_z\right)+\cos\left(2pu_y-2qu_z\right)\right] \\ & + c_7\left[\cos\left(pu_y+3qu_z\right)+\cos\left(pu_y-3qu_z\right)\right] + c_8\left[\cos 4qu_z\right] \\ & + a_1\left[\sin 2pu_y\right] + a_2\left[\sin\left(pu_y+qu_z\right)+\sin\left(pu_y-qu_z\right)\right] \\ & + a_4\left[\sin 4pu_y\right] + a_5\left[\sin\left(3pu_y+qu_z\right)+\sin\left(-3pu_y+qu_z\right)\right] \\ & + a_6\left[sin\left(2pu_y+2qu_z\right)+\sin\left(2pu_y-2qu_z\right)\right] + a_7\left[\sin\left(pu_y\right.\right. \\ & \left.\left.+3qu_z\right)+\sin\left(pu_y-3qu_z\right)\right]\Big]\end{aligned} \tag{1}$$

where u_y and u_z are the displacements induced by screw and edge dislocations, respectively. $p = 2\pi/b$ and $q=2\pi/\sqrt{3}b$.

Moreover, the dislocation width ξ could be calculated as [26].

$$\xi = \frac{K}{2}S_{44}\Delta d \tag{2}$$

where Δd is the spacing of adjacent atomic planes along the slip direction in a perfect bcc crystal. For a dislocation with $\vec{b_1}$=a/2 < 111 > , $\Delta d = \frac{\sqrt{3}a}{4}$, with a as the lattice parameter of the bcc crystal, $K = \frac{R}{S_{44}}$, where $R = \left[\frac{S_{11}S_{44}}{S_{11}S_{44}-S_{15}^2}\right]^{1/2}$, $S_{11} = \frac{1}{6}\left[\frac{1}{C_{11}-C_{12}}+\frac{1}{C_{44}}+\frac{9}{2(C_{11}+2C_{12}+C_{44})}\right]$, $S_{44} = \frac{1}{3}\left[\frac{4}{C_{11}-C_{12}}+\frac{1}{C_{44}}\right]$, $S_{15} = -\frac{\sqrt{2}}{6}\left[\frac{2}{C_{11}-C_{12}}-\frac{1}{C_{44}}\right]$, S_{ij} is the modified elastic compliance (by definition S_{ij}=S_{ij}-$S_{i3}S_{j3}/S_{33}$, where S_{ij} is the elastic compliance referred to the coordinate system) [26]. For a dislocation

with $\overrightarrow{b_2}$=a/2 < 110 >, $\Delta d = \frac{\sqrt{2}a}{4}$, $K = \frac{1}{3}\left[2\left(\frac{C_{12}}{C_{11}}\right)+1\right]K_e$, where $K_e = \frac{\overline{C_{12}}+C_{12}}{C_{12}}\left[\frac{C_{11}C_{44}(\overline{C_{12}}-C_{12})}{\overline{C_{12}}+C_{12}+2C_{44}}\right]^{0.5}$, and $\overline{C_{12}} = [\frac{1}{2} \quad C_{11} \quad (C_{11}+C_{12}+C_{44})]^{0.5}$, C_{ij} is the elastic constant of bcc crystal [26].

Peierls stress (τ_p) is defined as the critical resolved shear stress required to resist dislocation motion in a single crystal metal, whereas the yield strength of a bcc polycrystal metal can be predicted by [28,29].

$$\sigma_y = M\tau_y = \frac{1}{3}M\tau_p \tag{3}$$

where M= 2.733 [30]. Under the narrow core approximation (i.e., the width of dislocation core is in the order of one or two atomic spacing [31]) of the revised Peierls-Nabarro model [16], the Peierls stress can be calculated as

$$\tau_p = \frac{\Delta d}{\pi\xi}\max\{\frac{d\gamma(\mu)}{d\mu}\sin^2(\frac{\pi\mu}{b})\} \tag{4}$$

from the GSFE surface of bcc metals. The dislocations in bcc metals are usually classified as narrow-core dislocations [32–34]. Consequently, we applied the narrow core approximation of the revised Peierls-Nabarro model [16] to predict the Peierls stress required for dislocation slip in bcc HEAs.

It should be mentioned that the revised Peierls-Nabarro model can be directly applied only to predict the mobility of the dislocations with a planar core. In bcc metals, the screw dislocations are found to have a nonplanar core structure which is responsible for the observed non-glide stress effect on plastic flow [35–41]. To address this issue, Ngan et al. proposed a generalized Peierls-Nabarro model to treat the three-fold core structure of screw dislocations in bcc metal [42] and further derived that the Peierls stress τ_p for the screw dislocations with non-planar core would exhibit a $1/\cos^2\chi$ relation with respect to the orientation of the maximum resolved shear stress plane (i.e., the value of angle χ varies between $-30°$ and $30°$) [43]. Consequently, the Peierls stress of screw dislocations is calculated in this study to be in a range from $\frac{\Delta d}{\pi\xi}\max\{\frac{d\gamma(\mu)}{d\mu}\sin^2(\frac{\pi\mu}{b})\}$ to $\frac{1}{\cos^2 30°}\frac{\Delta d}{\pi\xi}\max\left\{\frac{d\gamma(\mu)}{d\mu}\sin^2(\frac{\pi\mu}{b})\right\}$ from the GSFE surface of bcc metals.

3.2. Predicted lattice parameters and elastic constants

We performed the DFT calculations to predict the equilibrium lattice parameters and elastic constants of the single crystal of bcc MoNbTaW, MoNbTaV, AlCoCrFeNi, and AlCoCrFeNiZr$_{0.3}$ HEAs. Modeling the bulk crystal of each alloy with the specified molar composition, we used the Alloy Theoretic Automated Toolkit (ATAT) code [44] to generate special quasi-random structures which mimic the element distribution in a random alloy. Two examples of the modeled bulk crystal structures of bcc HEAs are shown in Fig. 1. The equilibrium lattice parameter of these HEAs was determined by finding the minimum energy state as a function of the lattice parameter, whereas the elastic constants C_{11}, C_{12}, and C_{44} of these HEAs were derived from the energy curves obtained by applying the equal-axis volume expansion strain and volume conserving shear strains to the modeled bcc HEA crystal [45]. We present our predictions for bulk crystal of the four HEAs in Table 1. It is shown that the predictions agree well with the computational and experimental values from the literature.

Furthermore, we gave in Table 2 the predicted dislocation width ξ of both edge and screw dislocations in bcc MoNbTaW, MoNbTaV, AlCoCrFeNi, and AlCoCrFeNiZr$_{0.3}$ HEAs. Our predictions confirm that the narrow-core approximation is applicable to the dislocations in these four bcc HEAs. Moreover, the predicted dislocation widths of MoNbTaV are found to be slightly lower than those of MoNbTaW with the change of constituent W to V, and the dislocation widths of AlCoCrFeNiZr$_{0.3}$ are also slightly lower than those of AlCoCrFeNi with the addition of constituent Zr.

3.3. Predicted generalized stacking fault energy surface

The generalized stacking fault energy (GSFE) surface is believed to govern the dislocation mobility in bcc metals [35]. Hence, we further used the DFT method to predict the GSFE surfaces of bcc MoNbTaW, MoNbTaV, AlCoCrFeNi, and AlCoCrFeNiZr$_{0.3}$ HEAs. We used a twelve-layer slab containing 96 atoms for modeling the (112) GSFE surface of MoNbTaW and MoNbTaV HEAs, whereas a ten-layer (112) slab containing 80 atoms for AlCoCrFeNi and AlCoCrFeNiZr$_{0.3}$ HEAs. Some example structures on the (112) GSFE surface of bcc MoNbTaW alloy are illustrated in Fig. 2.

In this study, we computed the two-dimensional (112) GSFE surface by rigidly slipping the top half crystal on (112) plane by a displacement, whose vector could be decomposed along two basis Burgers vectors $\overrightarrow{b_1}$=a/2 < 111 > and $\overrightarrow{b_2}$=a/2 < 110 >. In total, we constructed thirty-six slipped crystal structures corresponding to a 2D grid in (112) with uniform increments of $\overrightarrow{b_1}/5$ and $\overrightarrow{b_2}/5$ along the two basis vectors. At each slip displacement, we computed the energies of the slipped crystal optimized using the DFT method. Furthermore, we applied the least square method to best fit the thirty-six DFT datapoints to the mathematical formula given in Eq. (1) and thus predict the (112) GSFE surface of the four bcc HEAs.

The fitted (112) GSFE surfaces for four bcc HEAs are plotted in Fig. 3 and Fig. 4. Points (0, 0) in these figures represent the perfect bcc crystal as shown in Fig. 2(a) and (f), whereas points (0.5, 0.0) and (0.0, 0.5) in the figures correspond to the half crystal slipped by $1/2\overrightarrow{b_1}$ and $1/2\overrightarrow{b_2}$ on (112) as shown in Fig. 2(c) and (h), respectively. It can be seen that no stable planar defect state appears on the (112) GSFE surface of these bcc HEAs, different from the GSFE curves of fcc HEAs showing stable intrinsic stacking faults [15]. Moreover, the calculated (112) GSFE surfaces exhibit clear asymmetry with respect to < 111 > direction, which qualitatively indicates the twinning and the anti-twinning slip asymmetry of bcc crystal [36].

In addition, our results in Fig. 3 and Fig. 4 indicate that the calculated (112) GSFE of bcc HEAs would change with their chemical

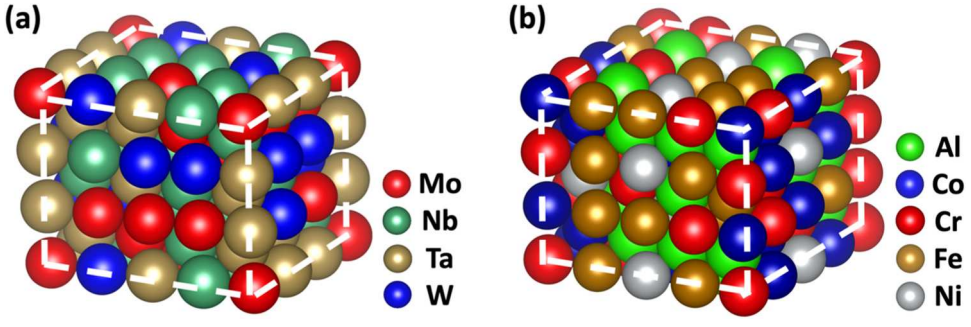

Fig. 1. Atomistic structures of the modeled bulk crystal of (a) quaternary MoNbTaW and (b) quinary AlCoCrFeNi HEAs with a bcc lattice structure.

Table 1
DFT predicted equilibrium lattice parameter a (in unit of Å), elastic constants C_{11}, C_{12}, and C_{44} (in unit of GPa) of four bcc HEAs. Experimental and computational values from the literature are included for comparison.

		MoNbTaW	MoNbTaV	AlCoCrFeNi	$AlCoCrFeNiZr_{0.3}$
a	This work	3.24	3.20	2.86	2.89
	Computational	3.25 [46]	3.21 [47]		
	Experimental	3.22 [7]	3.21[47]	2.91 [9]	2.95 [9]
C_{11}	This work	365	305	209	213
	Computational	371 [46]	301 [14]	214 [48]	
C_{12}	This work	161	135	137	126
	Computational	160 [46]	144 [14]	135 [48]	
C_{44}	This work	72	57	165	163
	Computational	69 [46]	63 [14]	167 [48]	

Table 2
Predicted core-widths of the screw dislocation (with a Burgers vector $\vec{b_1}$=a/2 <111 >) and edge dislocation (with a Burgers vector $\vec{b_2}$=a/2 <110 >) in four bcc HEAs using the DFT data in Table 1.

	MoNbTaW	MoNbTaV	AlCoCrFeNi	$AlCoCrFeNiZr_{0.3}$
screw	$0.52b_1$	$0.50b_1$	$0.59b_1$	$0.57b_1$
edge	$0.66b_2$	$0.65b_2$	$1.19b_2$	$1.06b_2$

composition. The highest fault energy in the (112) GSFE was found to increase from 4873 mJ/m^2 for MoNbTaW to 5191 mJ/m^2 for MoNbTaV with a change of constituent W to V and increase from 5269 mJ/m^2 for AlCoCrFeNi to 5835 mJ/m^2 for $AlCoCrFeNiZr_{0.3}$ with addition of constituent Zr. It should be mentioned that local chemical composition variation could affect the values of our predicted GSFE. To quantify this effect, we have predicted the fault energy at a specified displacement point (0.5, 0.5) on three different (112) planes with slightly different compositions for each bcc HEA. It was found that local composition variation around stoichiometry only causes an error less than 1.0% in the calculated value of GSFE.

3.4. Predicted yield strength

From the calculated (112) GSFE surfaces, we further predicted the Peierls stress (τ_p) required for dislocation slip in the four bcc HEAs using the revised Peierls-Nabarro model.[16] The results are presented in Table 3. On the two-dimensional (112) GSFE surface, we computed the Peierls stress as $\tau_p = \max|\vec{g}|$. The vector as expressed in Eq. (5a) was used to compute the minimum value of τ_p whereas the vector given in Eq. (5b) was used to compute the maximum value of τ_p.

$$\vec{g} = \left(\left(\frac{\Delta d_1}{\pi\xi_1}\frac{\partial\gamma(f_1,f_2)}{\partial f_1}\right)\sin^2\left(\frac{\pi f_1}{b_1}\right), \left(\frac{\Delta d_2}{\pi\xi_2}\frac{\partial\gamma(f_1,f_2)}{\partial f_2}\right)\sin^2\left(\frac{\pi f_2}{b_2}\right)\right) \quad (5a)$$

$$\vec{g} = \left(\left(\frac{1}{\cos^2 30^\circ}\frac{\Delta d_1}{\pi\xi_1}\frac{\partial\gamma(f_1,f_2)}{\partial f_1}\right)\sin^2\left(\frac{\pi f_1}{b_1}\right), \left(\frac{\Delta d_2}{\pi\xi_2}\frac{\partial\gamma(f_1,f_2)}{\partial f_2}\right)\sin^2\left(\frac{\pi f_2}{b_2}\right)\right) \quad (5b)$$

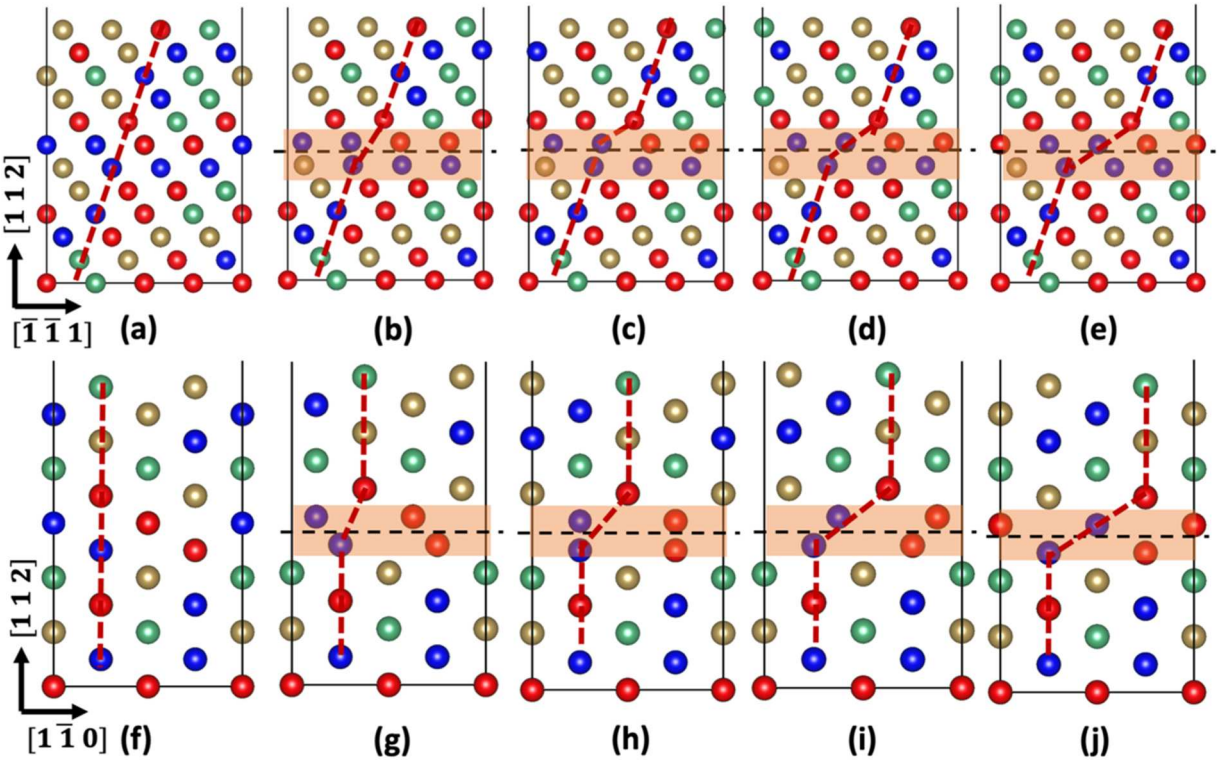

Fig. 2. Atomic structure of a simulation slab consisting of sequentially packed (112) atomic layers to model relative slip on (112) plane of bcc MoNbTaW HEA. The slip along [$\bar{1}$1 1] is depicted as (a) a perfect bcc crystal displaced by (b) $1/4\vec{b_1}$, (c) $1/2\vec{b_1}$, (d) $3/4\vec{b_1}$, and (e) $\vec{b_1}$. Here, $\vec{b_1}$=a/2 < 111 > . The slip along [1$\bar{1}$0] is shown as (f) a perfect bcc crystal displaced by (g) $1/4\vec{b_2}$, (h) $1/2\vec{b_2}$, (i) $3/4\vec{b_2}$, and (j) $\vec{b_2}$. Here, $\vec{b_2}$=a/2 < 110 > . In this figure, the red, green, brown, and blue balls represent Mo, Nb, Ta, and W atoms, respectively.

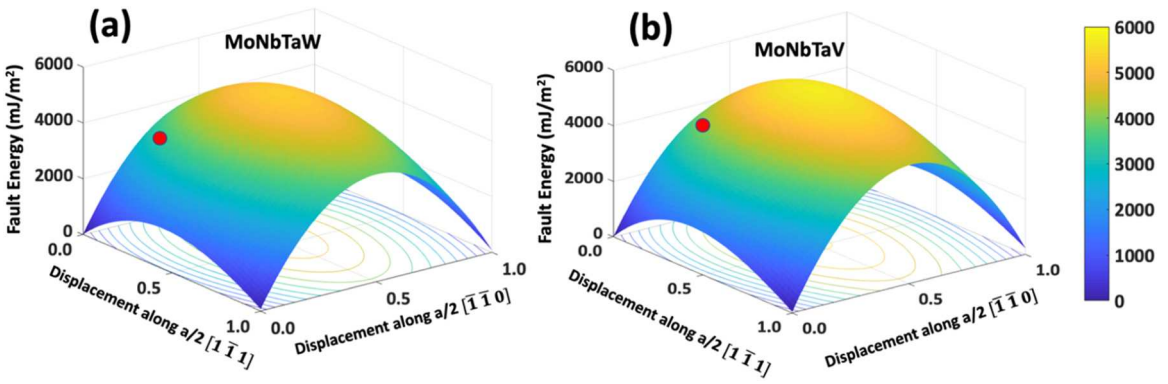

Fig. 3. Predicted (112) GSFE surface of (a) MoNbTaW and (b)MoNbTaV HEAs. The red dots indicate the location having the maximum gradient on the surface.

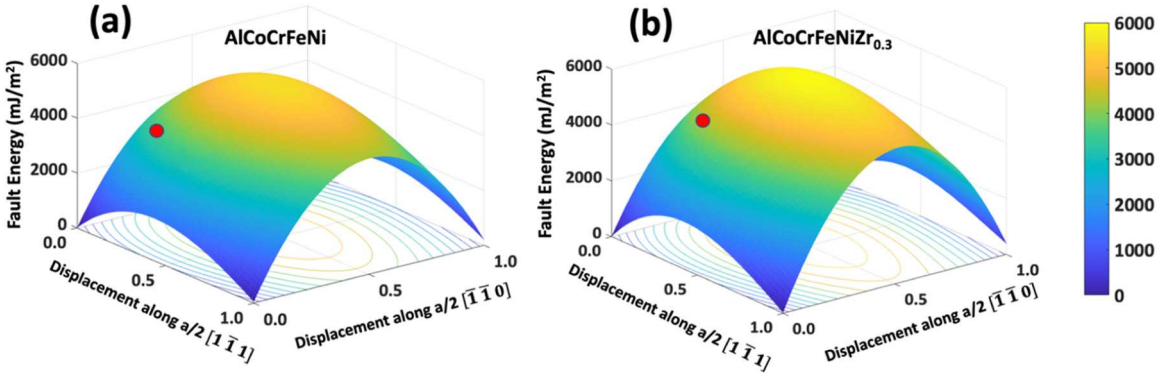

Fig. 4. Predicted (112) GSFE surface of (a) AlCoCrFeNi and (b) $AlCoCrFeNiZr_{0.3}$ HEAs. The red dots indicate the location having the maximum gradient on the surface.

Table 3
Predicted range of Peierls stress τ_p (in unit of MPa) of four bcc single crystal HEAs.

	MoNbTaW	MoNbTaV	AlCoCrFeNi	$AlCoCrFeNiZr_{0.3}$
τ_p	1115~1154	1622~1645	1474~1502	1883~1937

Where, $\Delta d_1 = \frac{\sqrt{3}}{4}a$ and $\Delta d_2 = \frac{\sqrt{2}}{4}a$ are the spacing of adjacent atomic planes along the slip direction $< 111 >$ and $< 110 >$, respectively, in a perfect bcc crystal, ξ_1 and ξ_2 are the width of the dislocation with Burger vector $\vec{b_1}$=a/2 $< 111 >$ and $\vec{b_2}$=a/2 $< 110 >$, respectively. The maximum gradient location on the (112) GSFE surface (i.e., where the minimal value of the Peierls stress are determined) of the four bcc HEAs are marked in Figs. 3 and 4. Furthermore, the yield strength of the four bcc HEAs in their polycrystal form were predicted by Eq. (3).

Our results in Table 4 show a good agreement between our model predictions with experimentally measured values, having a discrepancy ranging from 0.6% (for $AlCoCrFeNiZr_{0.3}$) to 2.4% (for MoNbTaV). Moreover, our model predicted yield strength of MoNbTaW alloy is found to have less discrepancy within 2.3% as compared to the experimental value (i.e.,1058 MPa) than that calculated from the misfit volume variation model [14] showing a difference of 7.8%.

Table 4
Predicted yield strength (in unit of MPa) of four bcc polycrystal HEAs. Experimental and computational values from the literature are included for comparison.

	MoNbTaW	MoNbTaV	AlCoCrFeNi	$AlCoCrFeNiZr_{0.3}$
This work	1034	1489	1356	1740
Experimental	1058 [6]	1525 [4]	1330 [9]	1750 [9]
Computational	975 [14]			

3.5. Discussion

Both experimental and our computational results in Table 4 show that the yield strength of MoNbTaV is higher than that of MoNbTaW with the change of constituent W to V, and the yield strength of $AlCoCrFeNiZr_{0.3}$ is higher than that of AlCoCrFeNi with the addition of constituent Zr. Quantitatively, the difference between the yield strengths of MoNbTaV and MoNbTaW HEAs was predicted by our model to be 455 MPa, which is very close to the experimental value of 467 MPa, whereas the difference between the yield strengths of $AlCoCrFeNiZr_{0.3}$ and AlCoCrFeNi HEAs was predicted to be 384 MPa, which is also comparable to the experimental value of 420 MPa. Consequently, our model provides a computational approach to quantify the dependency of the yield strength of bcc HEAs on their chemical composition.

Furthermore, some insights can be gained regarding how the yield strength would change with the chemical composition of bcc HEAs from this study. Based on the employed Peierls-Nabarro model, higher Periels stress and yield strength are the result of larger lattice resistance to dislocation slip. It has been proposed that atomic-radius mismatch is an important parameter to quantify the degree of lattice distortion and describe the solid-solution strengthening in HEAs [49]. To examine this concept, we have further calculated the equilibrium lattice parameters of all the constituent elements in bcc structure using the DFT method. The bcc lattice parameters are predicted to be 3.16 Å for Mo, 3.31 Å for Nb, 3.32 Å for Ta, 3.19 Å for W, and 3.00 Å for V, showing much smaller atomic radius of V as compared to those of the other four constituent elements. Using the same computational approach given in Ref. [49], we calculated the atomic-radius mismatch to be 2.3% for MoNbTaW and

4.4% for MoNbTaV using our calculated bcc lattice parameters. Moreover, the bcc lattice parameters are predicted to be 3.24 Å for Al, 2.83 Å for Fe, 2.81 Å for Co, 2.87 Å for Cr, 2.80 Å for Ni and 3.58 Å for Zr, showing much larger atomic radius of Zr as compared to those of the other five constituent elements. The atomic-radius mismatch is thus calculated to be 5.0% for AlCoCrFeNi and 6.8% for $AlCoCrFeNiZr_{0.3}$. Consequently, our analysis reveals a correlation between the atomic-radius mismatch (i.e., degree of lattice distortion) and the calculated yield strength of the two bcc HEA systems. Namely, larger atomic-radius mismatch would lead to higher yield strengths for the bcc HEAs with a systematic composition change.

4. Conclusion

In this study, we have developed a first principles based computational approach to predict the yield strength of bcc structured HEAs. Using the developed computational method based on the revised Peierls-Nabarro model, we are able to predict the Peierls stress required to slip the dislocations with both edge and screw characters in bcc HEAs. All the input data, including equilibrium lattice parameter, elastic constants, and two-dimensional (112) GSFE surface of bcc HEA, were calculated using the first-principles DFT method.

We further applied the computational approach to predict the yield strength of quaternary MoNbTaW, MoNbTaV, quinary AlCoCrFeNi, and senary $AlCoCrFeNiZr_{0.3}$ HEAs, all with a bcc crystal structure. Our predicted yield strength of these four bcc HEAs are found to agree well with experimentally measured values, exhibiting a difference ranging from 0.6% for $AlCoCrFeNiZr_{0.3}$ to 2.4% for MoNbTaV. Moreover, as compared to experimental data, our computational model accurately quantified the changes in the yield strength from MoNbTaW to MoNbTaV with the change of constituent W to V, and from AlCoCrFeNi to $AlCoCrFeNiZr_{0.3}$ with the addition of 6 at% Zr. Our model analysis suggests that increasing atomic-radius mismatch through systematically introducing either much smaller or much larger constituents could lead to higher room-temperature yield strengths of bcc HEAs.

Therefore, this study presents an accurate and reliable computational approach to explore the relation between the chemical composition and mechanical properties of bcc HEAs for further design of HEAs to have optimal mechanical properties. Additionally, the presented computational method sets up a theoretical framework extendable to predict the high-temperature yield strength and low-temperature ductility of bcc HEAs.

CRediT authorship contribution statement

Siming Zhang: Investigation, Method development, Data curation, Writing– original draft. **Guofeng Wang:** Conceptualization, Supervision, Writing – review & editing.

Declaration of Competing Interest

The authors declare that they have no known competing financial interests or personal relationships that could have appeared to influence the work reported in this paper.

Data availability

Data will be made available on request.

Acknowledgements

Financial support for this research provided by the National Science Foundation (NSF) (grant number DMR 1905572) is gratefully acknowledged. This research was also supported in part by the University of Pittsburgh Center for Research Computing, RRID: SCR_022735, through the computer resources provided. Specifically, this work used the H2P cluster, which is supported by NSF award number OAC-2117681.

References

[1] S. Wei, S.J. Kim, J. Kang, Y. Zhang, Y. Zhang, T. Furuhara, E.S. Park, C.C. Tasan, Natural-mixing guided design of refractory high-entropy alloys with as-cast tensile ductility, Nat. Mater. 19 (2020) 1175–1181, https://doi.org/10.1038/s41563-020-0750-4.
[2] J.-W. Yeh, S.-K. Chen, S.-J. Lin, J.-Y. Gan, T.-S. Chin, T.-T. Shun, C.-H. Tsau, S.-Y. Chang, Nanostructured high-entropy alloys with multiple principal elements: novel alloy design concepts and outcomes, Adv. Eng. Mater. 6 (2004) 299–303, https://doi.org/10.1002/adem.200300567.
[3] E.P. George, W.A. Curtin, C.C. Tasan, High entropy alloys: a focused review of mechanical properties and deformation mechanisms, Acta Mater. 188 (2020) 435–474, https://doi.org/10.1016/j.actamat.2019.12.015.
[4] F. Liu, P.K. Liaw, Y. Zhang, Recent progress with BCC-Structured high-entropy alloys, Metals 12 (2022) 501, https://doi.org/10.3390/met12030501.
[5] E. Mak, Y. Bin, W.A. Curtin, A ductility criterion for bcc high entropy alloys, J. Mech. Phys. Solids 152 (2021), 104389, https://doi.org/10.1016/j.jmps.2021.104389.
[6] O.N. Senkov, G.B. Wilks, D.B. Miracle, C.P. Chuang, P.K. Liaw, Refractory high-entropy alloys, Intermetallics 18 (2010) 1758–1765, https://doi.org/10.1016/j.intermet.2010.05.014.
[7] O.N. Senkov, G.B. Wilks, J.M. Scott, D.B. Miracle, Mechanical properties of $Nb_{25}Mo_{25}Ta_{25}W_{25}$ and $V_{20}Nb_{20}Mo_{20}Ta_{20}W20$ refractory high entropy alloys, Intermetallics 19 (2011) 698–706, https://doi.org/10.1016/j.intermet.2011.01.004.
[8] Z.D. Han, N. Chen, S.F. Zhao, L.W. Fan, G.N. Yang, Y. Shao, K.F. Yao, Effect of Ti additions on mechanical properties of NbMoTaW and VNbMoTaW refractory high entropy alloys, Intermetallics 84 (2017) 153–157, https://doi.org/10.1016/j.intermet.2017.01.007.
[9] J. Chen, P. Niu, Y. Liu, Y. Lu, X. Wang, Y. Peng, J. Liu, Effect of Zr content on microstructure and mechanical properties of AlCoCrFeNi high entropy alloy, Mater. Des. 94 (2016) 39–44, https://doi.org/10.1016/j.matdes.2016.01.033.
[10] N. Malatji, T. Lengopeng, S. Pityana, A.P.I. Popoola, Microstructural, mechanical and electrochemical properties of AlCrFeCuNiWx high entropy alloys, J. Mater. Res. Technol. 11 (2021) 1594–1603, https://doi.org/10.1016/j.jmrt.2021.01.103.
[11] Y. Huang, J. Gao, S. Wang, D. Guan, Y. Xu, X. Hu, W.M. Rainforth, Q. Zhu, I. Todd, Influence of tantalum composition on mechanical behavior and deformation mechanisms of TiZrHfTax high entropy alloys, J. Alloy. Compd. 903 (2022), 163796, https://doi.org/10.1016/j.jallcom.2022.163796.
[12] G. Ji, Z. Zhou, F. Meng, Xiao Yang, R. Sheng, J. Qiao, P.K. Liaw, M. Li, L. Jiang, S. Chen, Y. Tong, Effect of Zr addition on the local structure and mechanical properties of Ti–Ta–Nb–Zr refractory high-entropy alloys, J. Mater. Res. Technol. 19 (2022) 4428–4438, https://doi.org/10.1016/j.jmrt.2022.06.160.
[13] G. Vazquez, P. Singh, D. Sauceda, R. Couperthwaite, N. Britt, K. Youssef, D. D. Johnson, R. Arróyave, Efficient machine-learning model for fast assessment of elastic properties of high-entropy alloys, Acta Mater. 232 (2022), 117924, https://doi.org/10.1016/j.actamat.2022.117924.
[14] F. Maresca, W.A. Curtin, Mechanistic origin of high strength in refractory BCC high entropy alloys up to 1900K, Acta Mater. 182 (2020) 235–249, https://doi.org/10.1016/j.actamat.2019.10.015.
[15] S. Zhang, G. Wang, Predicting mechanical properties of high entropy alloys with face centered cubic structure from first principles calculations, Mater. Today Commun. 32 (2022), 104059, https://doi.org/10.1016/j.mtcomm.2022.104059.
[16] B. Joos, M.S. Duesbery, The peierls stress of dislocations: an analytic formula, Phys. Rev. Lett. 78 (1997) 266–269, https://doi.org/10.1103/PhysRevLett.78.266.
[17] V. Vitek, Intrinsic stacking faults in body-centred cubic crystals, Philos. Mag. 18 (1968) 773–786, https://doi.org/10.1080/14786436808227500.
[18] G. Kresse, J. Furthmuller, Efficient iterative schemes for ab initio total-energy calculations using a plane-wave basis set, Phys. Rev. B 54 (1996) 11169–11186, https://doi.org/10.1103/PhysRevB.54.11169.
[19] G. Kresse, D. Joubert, From ultrasoft pseudopotentials to the projector augmented-wave method, Phys. Rev. B 59 (1999) 1758–1775, https://doi.org/10.1103/PhysRevB.59.1758.
[20] J.P. Perdew, K. Burke, M. Ernzerhof, Generalized gradient approximation made simple, Phys. Rev. Lett. 77 (1996) 3865–3868, https://doi.org/10.1103/PhysRevLett.77.3865.
[21] H.J. Monkhorst, J.D. Pack, Special points for Brillouin-zone integrations, Phys. Rev. B 13 (1976) 5188–5192, https://doi.org/10.1103/PhysRevB.13.5188.
[22] D. Rodney, J. Bonneville, Dislocations, Phys. Metall. 16 (2014) 1591–1680, https://doi.org/10.1016/B978-0-444-53770-6.00016-2.
[23] F. Wang, G.H. Balbus, S. Xu, Y. Su, J. Shin, P.F. Rottmann, K.E. Knipling, J. C. Stinville, L.H. Mills, O.N. Senkov, I.J. Beyerlein, T.M. Pollock, D.S. Gianola, Multiplicity of dislocation pathways in a refractory multiprincipal element alloy, Science 370 (2020) 95–101, https://doi.org/10.1126/science.aba3722.
[24] C. Lee, F. Maresca, R. Feng, Y. Chou, T. Ungar, M. Widom, K. An, J.D. Poplawsky, Y.C. Chou, P.K. Liaw, W.A. Curtin, Strength can be controlled by edge dislocations in refractory high-entropy alloys, Nat. Commun. 12 (2021) 5474, https://doi.org/10.1038/s41467-021-25807-w.
[25] Q. Zhang, R. Huang, X. Zhang, T. Cao, Y. Xue, X. Li, Deformation mechanisms and remarkable strain hardening in single-crystalline high-entropy-alloy micropillars/nanopillars, Nano Lett. 21 (2021) 3671–3679, https://doi.org/10.1021/acs.nanolett.1c00444.

[26] Y.T. Chou, G.T. Sha, Energy, stability, and peierls stress of glide dislocations in anisotropie BCC crystals, Metall. Mater. Trans. B 3 (1972) 2857–2863, https://doi.org/10.1007/BF02652853.
[27] G. Schoeck, The core structure of "001" dislocations in bcc metals, Philos. Mag. Lett. 76 (1997) 15–24, https://doi.org/10.1080/095008397179336.
[28] U.F. Kocks, The relation between polycrystal deformation and single-crystal deformation, Metall. Mater. Trans. B 1 (1970) 1121–1143, https://doi.org/10.1007/BF02900224.
[29] K.W. Siu, A. Ngan, Relation between yield stress and peierls stress, Phys. Status Solidi B 256 (2019), 1900107, https://doi.org/10.1002/pssb.201900107.
[30] J.M. Rosenberg, H.R. Piehler, Calculation of the taylor factor and lattice rotations for bcc metals deforming by pencil glide, Metall. Trans. 2 (1971) 257–259, https://doi.org/10.1007/BF02662666.
[31] A.J. Foreman, M.A. Jaswon, J.K. Wood, Factors controlling dislocation widths, Proc. Phys. Soc. A 64 (1951) 156–163, https://doi.org/10.1088/0370-1298/64/2/307.
[32] J.P. Hirth, J. Lothe. Theory of Dislocations, second edition.,, Wiley-Interscience Publication,, 1982.
[33] P. Follansbee, The Minerals, Metals & Materials Series, Springer, Cham,, 2022.
[34] C.N. Reid, Dislocation widths in anisotropic B.C.C. crystals, Acta Metall. 14 (1966) 13–16, https://doi.org/10.1016/0001-6160(66)90266-5.
[35] M.S. Duesbery, V. Vitek, Plastic anisotropy in b.c.c. transition metals, Acta Mater. 46 (1998) 1481–1492, https://doi.org/10.1016/S1359-6454(97)00367-4.
[36] G. Wang, A. Strachan, T. Çağın, W.A. Goddard II, Role of core polarization curvature of screw dislocations in determining the Peierls stress in bcc Ta: a criterion for designing high-performance materials, Phys. Rev. B 67 (2003), 140101, https://doi.org/10.1103/PhysRevB.67.140101.
[37] M.S. Duesbery, On non-glide stresses and their influence on the screw dislocation core in body-centred cubic metals I. the Peierls stress, Proc. R. Soc. A 392 (1984) 145–173, https://doi.org/10.1098/rspa.1984.0027.
[38] A. Kraych, E. Clouet, L. Dezerald, L. Ventelon, F. Willaime, D. Rodney, Non-glide effects and dislocation core fields in BCC metals, npj Comput. Mater. 5 (2019) 109, https://doi.org/10.1038/s41524-019-0247-3.
[39] V. Vitek, M. Mroveca, J.L. Bassani, Influence of non-glide stresses on plastic flow: from atomistic to continuum modeling, Mater. Sci. Eng. A 365 (2004) 31–37, https://doi.org/10.1016/j.msea.2003.09.004.
[40] R. Gröger, Which stresses affect the glide of screw dislocations in bcc metals, Philos. Mag. 94 (2014) 2021–2030, https://doi.org/10.1080/14786435.2014.904058.
[41] R. Gröger, V. Vitek, Impact of non-Schmid stress components present in the yield criterion for bcc metals on the activity of {110}<111> slip systems, Comput. Mater. Sci. 159 (2019) 297–305, https://doi.org/10.1016/j.commatsci.2018.12.021.
[42] A.H.W. Ngan, A generalized Peierls-Nabarro model for nonplanar screw dislocation cores, J. Mech. Phys. Solids 45 (1997) 903–921, https://doi.org/10.1016/S0022-5096(96)00125-1.
[43] A.H.W. Ngan, H.F. Zhang, A universal relation for the stress dependence of activation energy for slip in body-centered cubic crystals, J. Appl. Phys. 86 (1999) 1236–1244, https://doi.org/10.1063/1.370877.
[44] A. van de Walle, P. Tiwary, M. de Jong, D.L. Olmsted, M. Asta, A. Dick, D. Shin, Y. Wang, L.-Q. Chen, Z.-K. Liu, Efficient stochastic generation of special quasirandom structures, Calphad 42 (2013) 13–18, https://doi.org/10.1016/j.calphad.2013.06.006.
[45] P. Söderlind, O. Eriksson, J.M. Wills, A.M. Boring, Theory of elastic constants of cubic transition metals and alloys, Phys. Rev. B 48 (1993) 5844–5851, https://doi.org/10.1103/PhysRevB.48.5844.
[46] M.C. Gao, P. Gao, J.A. Hawk, L. Ouyang, D.E. Alman, M. Widom, Computational modeling of high-entropy alloys: structures, thermodynamics and elasticity, J. Mater. Res. 32 (2017) 3627–3641, https://doi.org/10.1557/jmr.2017.366.
[47] R.A. Romero, S. Xu, W. Jian, I.J. Beyerlein, C.V. Ramana, Atomistic simulations of the local slip resistances in four refractory multi-principal element alloys, Int. J. Plast. 149 (2022), 103157, https://doi.org/10.1016/j.ijplas.2021.103157.
[48] P. Sarswat, T. Smith, S. Sarkar, A. Murali, M. Free, Design and fabrication of new high entropy alloys for evaluating titanium replacements in additive manufacturing, Materials 13 (2020) 3001, https://doi.org/10.3390/ma13133001.
[49] L. Li, Q. Fang, J. Li, B. Liu, Y. Liu, P.K. Liaw, Lattice-distortion dependent yield strength in high entropy alloys, Mater. Sci. Eng. A 784 (2020), 139323, https://doi.org/10.1016/j.msea.2020.139323.